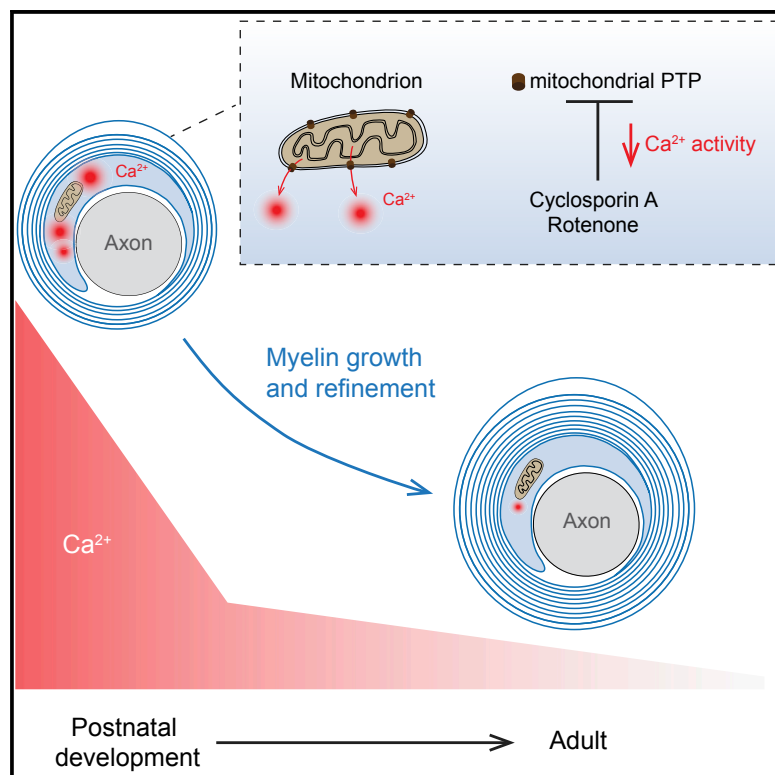


High-Frequency Microdomain Ca^{2+} Transients and Waves during Early Myelin Internode Remodeling

Graphical Abstract



Authors

Arne Battefeld, Marko A. Popovic,
Sharon I. de Vries, Maarten H.P. Kole

Correspondence

arne.battefeld@u-bordeaux.fr (A.B.),
m.kole@nin.knaw.nl (M.H.P.K.)

In Brief

Using epifluorescence imaging of oligodendrocytes during myelin development and remyelination, Battefeld et al. discovered that actively myelinating sheaths have high rates of local spontaneous calcium transients and propagating calcium waves. Myelin calcium transients are generated by the spontaneous activity of mitochondria in the non-compacted myelin, independently from neuronal activity.

Highlights

- Developing myelin sheaths show high rates of calcium transients and calcium waves
- Myelin calcium transients are independent from neuronal activity
- Adaxonal and paranodal myelin contained mitochondria
- Calcium transients require opening of mitochondrial permeability transition pores



High-Frequency Microdomain Ca^{2+} Transients and Waves during Early Myelin Internode Remodeling

Arne Battefeld,^{1,3,*} Marko A. Popovic,^{1,4} Sharon I. de Vries,¹ and Maarten H.P. Kole^{1,2,5,*}

¹Department of Axonal Signaling, Netherlands Institute for Neuroscience, Royal Netherlands Academy of Arts and Sciences, Meibergdreef 47, 1105 BA, Amsterdam, the Netherlands

²Cell Biology, Faculty of Science, University of Utrecht, Padualaan 8, 3584 CH, Utrecht, the Netherlands

³Present address: Institut des Maladies Neurodégénératives - CNRS UMR 5293, Université de Bordeaux, 146 rue Léo Saignat, 33000 Bordeaux, France

⁴Present address: Amsterdam UMC, Molecular Cell Biology and Immunology, Gustav Mahlerlaan 665, 1082 MK Amsterdam, the Netherlands

⁵Lead Contact

*Correspondence: arne.battefeld@u-bordeaux.fr (A.B.), m.kole@nin.knaw.nl (M.H.P.K.)

<https://doi.org/10.1016/j.celrep.2018.12.039>

SUMMARY

Ensheathment of axons by myelin is a highly complex and multi-cellular process. Cytosolic calcium (Ca^{2+}) changes in the myelin sheath have been implicated in myelin synthesis, but the source of this Ca^{2+} and the role of neuronal activity is not well understood. Using one-photon Ca^{2+} imaging, we investigated myelin sheath formation in the mouse somatosensory cortex and found a high rate of spontaneous microdomain Ca^{2+} transients and large-amplitude Ca^{2+} waves propagating along the internode. The frequency of Ca^{2+} transients and waves rapidly declines with maturation and reactivates during remyelination. Unexpectedly, myelin microdomain Ca^{2+} transients occur independent of neuronal action potential generation or network activity but are nearly completely abolished when the mitochondrial permeability transition pores are blocked. These findings are supported by the discovery of mitochondria organelles in non-compacted myelin. Together, the results suggest that myelin microdomain Ca^{2+} signals are cell-autonomously driven by high activity of mitochondria during myelin remodeling.

INTRODUCTION

The multi-lamellar myelin sheath around vertebrate axons is paramount for rapid and efficient saltatory conduction of the action potential and formed by a complex multi-cellular process (Nave and Werner, 2014). Myelination of neuronal networks in the brain develops rapidly after birth and is a lifelong process, with newly generated myelin sheaths continually integrated in the mature cortex even in mice 2 years of age (Fard et al., 2017; Hill et al., 2018; Hughes et al., 2018; Vincze et al., 2008; Young et al., 2013). Myelin develops from oligodendrocyte precursor cells (OPCs) that undergo terminal differentiation through a short intermediate phase, termed newly formed (or pre-myelinating) oligodendrocytes, and subsequently turn into mature myelinating oligodendrocytes (OLs) (Barres and Raff, 1999; Nishiyama et al., 2009; Zhang et al., 2014). Both OPC differentiation and stabilization of axo-glial contacts depend on neuronal activity and vesicle release from axons (Hines et al., 2015; Koudelka et al., 2016; Mensch et al., 2015; Wake et al., 2011). In early phases of myelin formation, glutamate release from axons triggered by neuronal activity has been shown instructive for myelin induction (Kukley et al., 2007; Stevens et al., 2002; Sun et al., 2016; Wake et al., 2011). Furthermore, there is converging evidence that the signaling pathways to increase myelin basic protein (MBP) translation and synthesis require intracellular Ca^{2+} changes in OPCs (Friess et al., 2016; Wake et al., 2011).

Although the mechanisms of Ca^{2+} signaling have been studied in OPCs (Friess et al., 2016; Haak et al., 2000, 2002; Kirischuk et al., 1995), little is known about Ca^{2+} signaling in early developing or mature myelin sheaths. Recent *in vivo* Ca^{2+} imaging of newly formed OLs in zebrafish revealed spontaneous Ca^{2+} events in myelin sheaths lasting 15–20 s correlated with both growth and calpain-mediated retraction of the myelin sheath (Baraban et al., 2018; Krasnow et al., 2018). Whether Ca^{2+} transients occur in mammalian myelin sheaths and can integrate neuronal activity at the temporal resolution of single action potentials, typically lasting only milliseconds, remains to be examined. Here, we used an OL-specific reporter mouse line to combine visually guided patch-clamp recordings with Ca^{2+} imaging of early developing and adult OLs in the gray matter of the somatosensory neocortex. Using a combination of electrophysiology, one-photon Ca^{2+} imaging with high sensitivity, electron microscopy (EM), and immunohistochemistry, we investigated Ca^{2+} in single OLs in the first postnatal months and characterized myelin Ca^{2+} transients in connected pairs of neurons and OLs. Our experiments revealed a remarkably high rate of brief (~1 s duration) microdomain Ca^{2+} transients and propagating Ca^{2+} waves in the cytoplasmic compartments of myelin. Microdomain Ca^{2+} transients required the spontaneous opening of the mitochondrial permeability transition pore (mPTP) but were independent of neuronal activity. These results suggest a model in which cell autonomous mitochondrial-driven Ca^{2+} homeostasis regulates myelin lipid biosynthesis and energy substrate production for radial and longitudinal refinement of the myelin sheath.



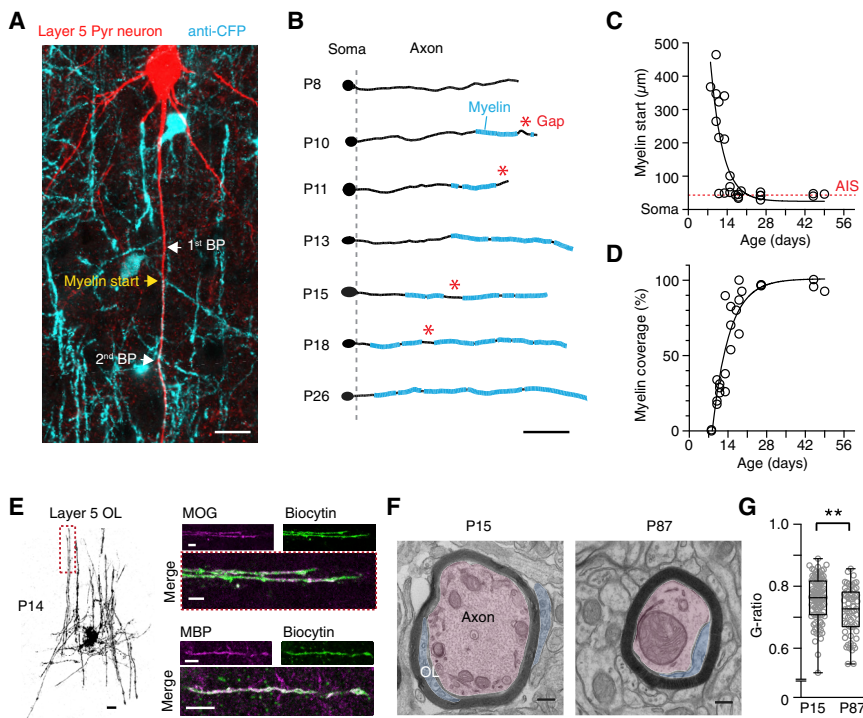


Figure 1. Radial and Longitudinal Myelin Development in the Somatosensory Cortex in the First Postnatal Weeks

(A) Fluorescence image of a layer 5 neuron in the somatosensory cortex (P15) of a PLP-ECFP mouse. The neuron was filled with biocytin (red) and co-labeled for ECFP (cyan) to identify OLs and myelinated segments. Start of myelin and branch-points (BPs) are indicated. Scale bar, 20 μm.

(B) Examples of reconstructed primary axon (black) overlaid with myelin segments (cyan). Scale bar, 100 μm. Asterisks indicate gaps larger than nodes of Ranvier.

(C) The start of the first myelinated segment moves closer to the axon initial segment (dotted line) within the third postnatal week. Data fit with a single exponential equation with a time constant of 4.4 days.

(D) Layer 5 axon myelination develops rapidly and reaches completion near P21. Data points represent individual axons and are corrected for an unmyelinated proximal length of 45 μm that includes the AIS. Data fit with a single exponential equation with a time constant of 6 days.

(E) Left: a P14 OL filled with biocytin. Right: post hoc staining of two OLs confirms that internodes are positive for MOG and MBP at P14. The dotted box (left) indicates the MOG-positive internode. Scale bars, 10 μm.

(F) Electron microscopy (EM) images of large axons in the somatosensory cortex during development (P15) and adulthood (P87).

OL cytoplasmic ridges (cyan) and neuron (red) are false colored. Scale bars, 200 nm.

(G) G-ratio measurements (inner axon diameter/outer diameter including myelin) reveals an average of 0.76 ± 0.01 at P14 ($n = 96$ axons) and a smaller g ratio at P87 ($n = 64$ axons; $p = 0.002$, Mann-Whitney test). Horizontal bar in the 25th to 75th percentile boxplot indicates the median and the error bars the maximum and minimum.

See also Figures S1 and S3.

RESULTS

Radial and Longitudinal Myelin Development in the Somatosensory Cortex in the First Postnatal Weeks

To characterize myelin development of the gray matter primary somatosensory layer 5 axons, we used a combination of single-axon tracing and myelin protein expression analysis by immunohistochemistry and EM (Figure 1). While the first myelin segments of layer 5 axons emerged near the corpus callosum at postnatal day 10 (P10), the first myelin internodes near the axon initial segment were formed approximately 1 week later (~P17 to P18; Figures 1A–1C), consistent with previous light and electron microscopic work (Vincze et al., 2008). Although internode length was similar across all periods (Figure S1A), large gaps between myelinated segments indicated that myelination was not complete until P18 (Figures 1B and 1D). At P14, enhanced cyan fluorescent protein (ECFP)-positive OLs had $\sim 35 \pm 8$ internodes ($n = 3$ OLs) and expressed the myelin specific proteins myelin oligodendrocyte glycoprotein (MOG; $n = 2$) and MBP ($n = 2$; Figure 1E). At this age, axons had a significantly thinner myelin sheath (i.e., a larger g ratio of 0.76 ± 0.01) compared to those in the adult cortex (g ratio = 0.72 ± 0.01 ; $p = 0.002$, Mann-Whitney test) suggesting that radial myelin growth continues after P15 (Figures 1F and 1G). During early development, the OL resting membrane potential depolarized

and input resistance decreased, reaching adult values around 4–5 weeks of age (Figures S1B–S1D). These data show that myelin wrapping around the layer 5 axon undergoes rapid longitudinal and radial refinement during the first postnatal weeks.

Myelin Ca²⁺ Transients and Ca²⁺ Waves during Early Development and Remyelination

To investigate Ca²⁺ in myelin sheaths we made acute brain slices prepared from reporter mice expressing ECFP under the OL-specific proteolipid protein (PLP) promoter (Battefeld et al., 2016; Hirrlinger et al., 2005) and targeted single ECFP-positive OLs between P12 and P111 (Figure S2A). During whole-cell recordings of ECFP-positive OLs in layers 5 and 6, the OLs were filled with OGB-1 for ~45 min before recording Ca²⁺ reporter fluorescence in internodes with a back-illuminated charge-coupled device (CCD) camera at 40 Hz (Figure 2A). Ca²⁺ changes appeared as transients restricted to small microdomains or as large-amplitude Ca²⁺ waves propagating longitudinally along the internode, clearly distinguishable with an average signal-to-noise ratio of 5.2 ± 0.6 ($n = 51$ events, $N = 12$ OLs) (Figures 2B, 2C, and S2B; Videos S1 and S2). Comparison of different sampling rates between 1 and 40 Hz revealed that higher rates were required to reliably identify the brief Ca²⁺ transients and analyze their properties and kinetics (Figure 2D). Although microdomain Ca²⁺ transients were of short half-width

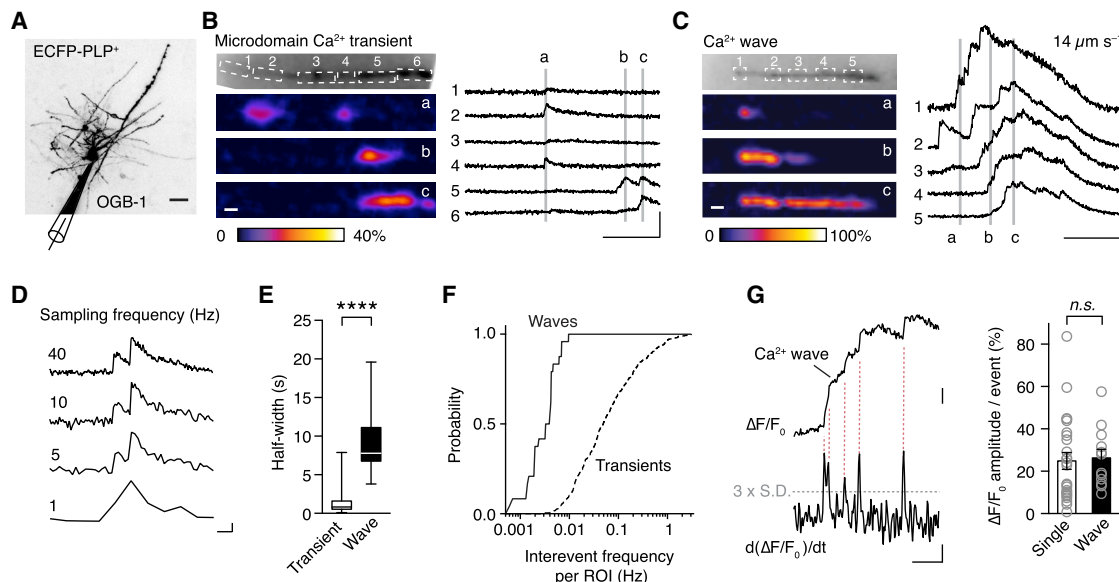


Figure 2. High-Frequency Microdomain Ca^{2+} Transients and Ca^{2+} Waves during Early Myelin Remodeling

(A) Confocal z projection of a live-scanned OL filled with 100 μM OGB-1. Scale bar, 20 μm .
(B and C) Left: Ca^{2+} transients (B) and wave (C) from two different OLs (scale bar, 5 μm). Right: Ca^{2+} traces with corresponding ROI locations (numbers) and time points (letters) as indicated in epifluorescence images (scale bars, 5 s and 30% $\Delta\text{F/F}$, B, and $\Delta\text{F/F}_0$, C).
(D) Comparison of different optical sampling frequencies. Scale bars, 1 s and 10% $\Delta\text{F/F}$.
(E) Half-width duration of myelin Ca^{2+} events is longer in waves ($n = 21$) compared with transients ($n = 421$; $p = 0.0001$, Mann-Whitney test). Boxplot indicates 25th and 75th percentiles, the horizontal bar in the box indicates the median, and error bars show the maximum and minimum.
(F) Cumulative probability plot of inter-event frequencies reveals that Ca^{2+} transients occur 50 times more often than Ca^{2+} waves (transients: $n = 418$ events, $n = 11$ OLs; waves: $n = 24$, $n = 14$ OLs; $p < 0.0001$, Kolmogorov-Smirnov test).
(G) Left: Ca^{2+} wave with expanded timescale reveals a summation of brief Ca^{2+} transients. By using the first derivative of the fluorescence (lower trace – $d(\Delta\text{F/F})/dt$), peak detection could be performed when fluorescence change was fastest (peak). Several transients are indicated (vertical dotted lines) and the cut-off set as $3 \times \text{SD}$ (horizontal dotted line). Scale bars, 10% $\Delta\text{F/F}_0$, 50% $\Delta\text{F/F} \times \text{s}^{-1}$, and 1 s. Right: summary data comparing the predicted amplitude of Ca^{2+} events within a wave to individual Ca^{2+} transients (five first events of five control OLs; $p = 0.42$, Mann-Whitney test). Mean \pm SEM.
See also Figure S2.

duration, lasting on average 1.3 ± 0.1 s, Ca^{2+} waves persisted significantly longer (on average 9.0 ± 0.8 s, $n = 12$ OLs; Figure 2E). Ca^{2+} transients were observed in the majority of imaged myelin sheaths (75% [160 of 216 sheaths], $n = 53$ OLs) and occurred ~ 50 times more frequently than Ca^{2+} waves (10% [20 of 216 sheaths]; Figure 2F). Further analysis revealed that Ca^{2+} waves were composed of multiple smaller Ca^{2+} transients (12 of 31 waves; Figure 2G). Ca^{2+} waves were not observed to propagate between different myelin sheaths of the same OL, suggesting that Ca^{2+} activity is independently regulated within internodes. Most events decayed within 3 s, with a half maximum duration of 1.6 s and a Ca^{2+} increase $< 15\%$ $\Delta\text{F/F}_0$ (Figures S2C–S2E). When corrected for the region of interest (ROI) size (events per micrometer), Ca^{2+} event probability was equally distributed along the internode ($48 \pm 5\%$ at the end tips, $52 \pm 5\%$ in the rest of the internode, $n = 365$ events from 23 internodes of 7 OLs; $p = 0.67$, paired t test).

Ca^{2+} imaging experiments from mice between 2 weeks and 3 months of age revealed that Ca^{2+} event frequency was highest in the earliest detectable ECFP-positive OLs in layers 5 and 6 (P12). Ca^{2+} activity rapidly attenuated within the first 2 weeks, after which little to no activity could be detected within the time frame of whole-cell recording (Figures 3A and 3B). Interestingly, the rate of developmental decrease in Ca^{2+} events mirrored the

change in myelin coverage of layer 5 pyramidal cell axons and the maturation of the intrinsic membrane properties of OLs (Figures 3B and S1). Indeed, the extent of myelin coverage was negatively correlated with the Ca^{2+} event frequency in the internodes ($r = -0.89$; Figure S3A) as well as the OL resting membrane potential, with Ca^{2+} event rate being highest in hyperpolarized OLs ($r = -0.89$; Figure S3B). Although microdomain Ca^{2+} transients were consistently observed between P13 and P43 ($n = 32$ OLs), large-amplitude Ca^{2+} waves occurred almost exclusively between P13 and P15 (93% [28 of 30 waves], $n = 14$ OLs), coinciding with a phase of rapid longitudinal remodeling of myelin (Figure 3C). Ca^{2+} spread along the internode was positively correlated with $\Delta\text{F/F}_0$ (Pearson $r = 0.51$, $p = 0.0001$, $N = 22$ OLs, $n = 391$ events; Figure 3D) but did not lead to membrane potential changes measured at the OL cell body ($p = 0.97$; Figure S3C).

To link the Ca^{2+} fluorescence changes to underlying signaling pathways, we measured the absolute baseline and spontaneous cytoplasmic Ca^{2+} concentration changes ($[\text{Ca}^{2+}]_i$) in myelin using the ratiometric Ca^{2+} indicator fura-2 (Figures S3D–S3F). These experiments revealed an internodal $[\text{Ca}^{2+}]_i$ of 49 ± 6 nM at rest (nine internodes, three OLs), similar to estimates in OPCs (Friess et al., 2016), and spontaneous microdomain Ca^{2+} transients were producing a $\Delta[\text{Ca}^{2+}]_i$ of ~ 19 nM (three internodes, two

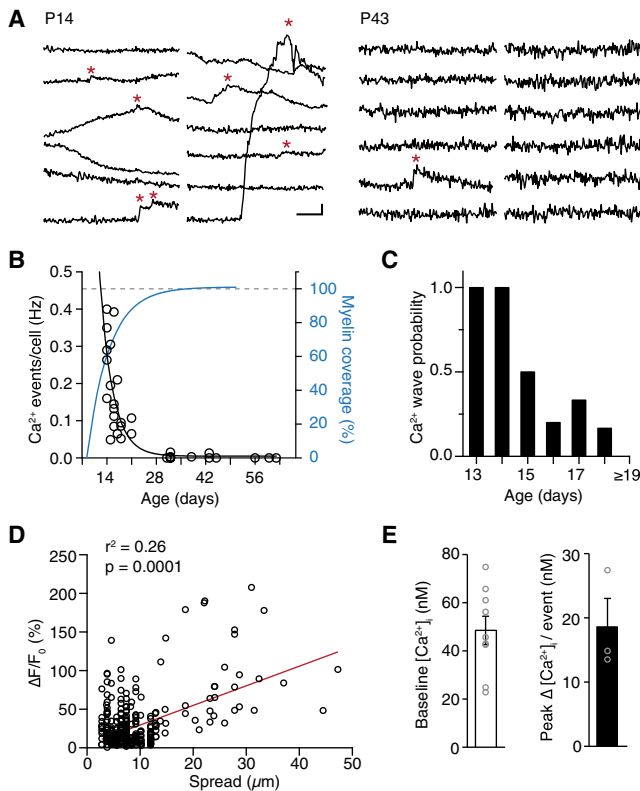


Figure 3. Ca^{2+} Events Attenuate during Myelin Maturation
(A) Example Ca^{2+} traces for two ages (P14 and P43). Note the large Ca^{2+} waves at P14. Scale bars, 10% $\Delta F/F_0$ and 1 s. Asterisks indicate Ca^{2+} events.
(B) Scatterplot of myelin Ca^{2+} events per OL (open black circles) revealing a rapid decrease until the third postnatal week. Dotted blue line represents the fit to myelin coverage of layer 5 axons (same fit as in Figure 1D).
(C) Probability of Ca^{2+} waves rapidly declines between P13 and P63. P13, 2 waves and 2 OLs; P14, 5 waves and 5 OLs; P15, 4 waves and 8 OLs; P16, 1 wave and 5 OLs; P17, 1 wave and 3 OLs; P18, 1 wave and 6 OLs; $\geq P19$, 0 waves and 13 OLs.
(D) Scatterplot of $\Delta F/F_0$ changes versus spatial spread shows a positive correlation ($n = 391$ events, $N = 22$ cells). Data fit with a linear function (red line).
(E) Left: bar plot for baseline intracellular internode Ca^{2+} concentration $[\text{Ca}^{2+}]_i$ ($n = 9$ internodes). Right: bar plot for Ca^{2+} peak change during Ca^{2+} transients ($n = 3$ internodes from $N = 3$ animals) obtained with ratiometric Ca^{2+} imaging from internodes. Data are presented as mean \pm SEM.

See also Figure S3.

OLs; Figure 3E). On the basis of our finding that Ca^{2+} waves are composed of two to seven events, we estimate that $\Delta[\text{Ca}^{2+}]_i$ during Ca^{2+} waves rises from ~ 90 to $\sim 200 \text{ nM}$, respectively, suggesting a large dynamic range in Ca^{2+} concentrations within the myelin sheath.

Because there is a strong age-dependent reduction in newly formed oligodendrocytes after myelin development (Fard et al., 2017), our low rate of Ca^{2+} events in myelin sheaths in adulthood may reflect a reduced probability to target newly formed OLs. We hypothesized that similar Ca^{2+} dynamics as observed during myelin maturation should occur during remyelination in adulthood. To test this, we used the cuprizone model, which effectively demyelinates hundreds of micrometers of the proximal

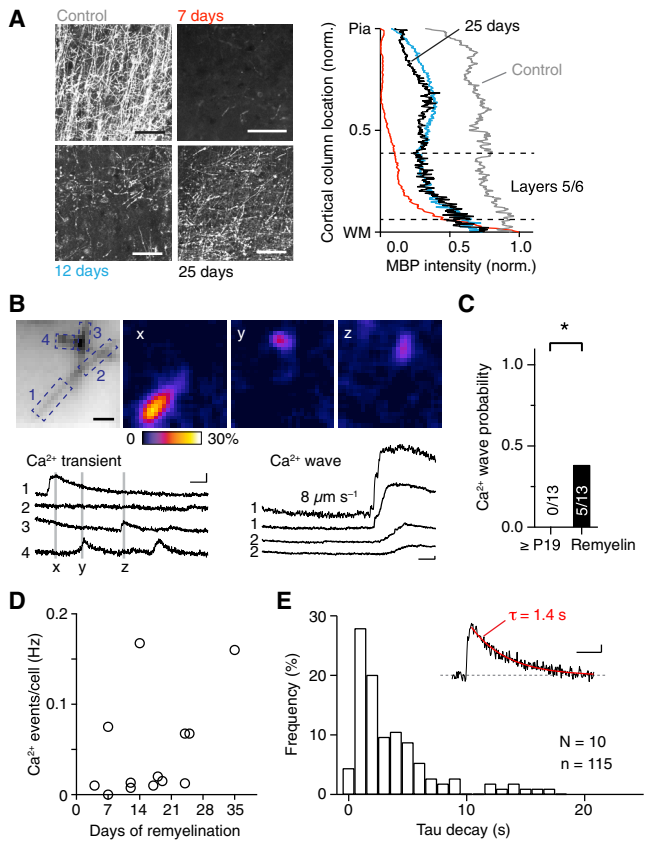


Figure 4. Remyelination Reactivates Ca^{2+} Microdomain Transients and Ca^{2+} Waves
(A) Left: representative MBP immunostainings of layer 5 in control and after 7, 12, and 25 days of remyelination. Scale bars, 50 μm . Right: normalized MBP intensity for the four stages plotted versus the normalized cortical column length. WM, white matter.
(B) Top: images of resting and frame subtracted fractional fluorescence change with time points indicated (x, y, z). Scale bar, 5 μm . Bottom: corresponding Ca^{2+} traces of the ROIs for transient Ca^{2+} events and Ca^{2+} waves from two different trials. The Ca^{2+} wave initiates at the end tip (ROI 1) and propagates toward the center of the sheath (ROI 2). Scale bars, 10% $\Delta F/F_0$ and 2 s.
(C) Ca^{2+} wave probability increases during remyelination ($p = 0.039$, Fisher exact test).
(D) Ca^{2+} event frequency is increased up to 35 days after remyelination onset.
(E) Histogram of the decay time constant for Ca^{2+} events during remyelination. Inset shows a typical Ca^{2+} event; scale bars, 5% $\Delta F/F_0$ and 1 s.

See also Figure S4.

part of the primary layer 5 axon after a 5 week cuprizone diet (Hamada and Kole, 2015), and then induced remyelination by terminating the cuprizone diet. Remyelination was variable across the cortical layers and still ongoing after 25 days of remyelination (Figure 4A), in line with previous data (Baxi et al., 2017; Clarner et al., 2012). We recorded from newly generated ECFP-expressing OLs in layers 5 and 6 and imaged internodal Ca^{2+} between 4 and 35 days of the remyelination phase (Figures 4B and S4A). These recordings showed that Ca^{2+} waves occurred in $\sim 40\%$ of the OLs (Figure 4C), and Ca^{2+} transients

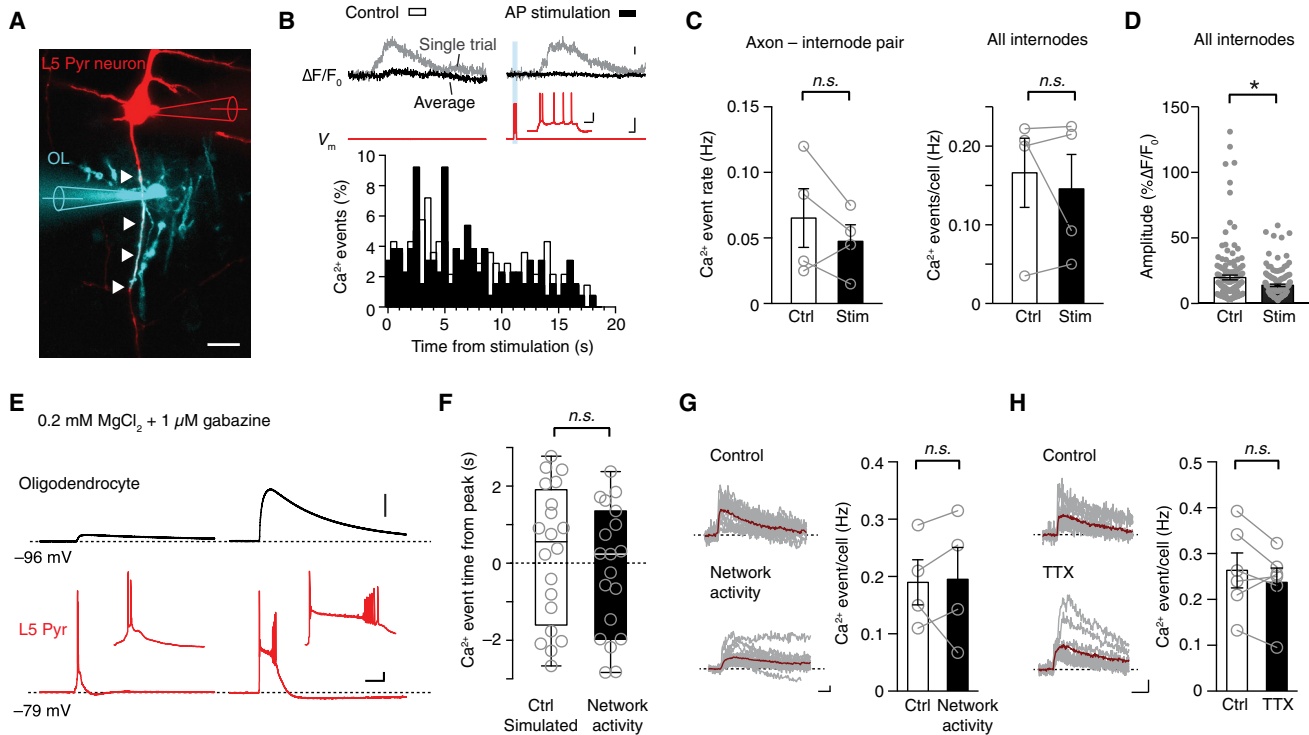


Figure 5. Myelin Microdomain Ca^{2+} Transients Are Independent of Neuronal Activity

(A) Confocal image of a simultaneous OL-neuron whole-cell recording (white arrowheads indicate shared axon). Scale bar, 20 μm .
(B) Top: example traces of the neuronal membrane potential (V_m , red) and myelin Ca^{2+} signals (same ROI) for control and stimulation. Bottom: histogram of events relative to the action potential (AP) stimulus at 0 s. Ca^{2+} events in control were aligned to the AP onset. Scale bars, 5% $\Delta F/F_0$, 30 mV, and 1 s. Inset: 30 mV and 0.1 s.
(C) Left: Ca^{2+} event frequency of single axon-internode pairs before and after stimulation ($p = 0.38$, Wilcoxon signed rank test; $n = 4$ paired recordings, $N = 3$ animals). Right: Ca^{2+} event frequency for all internodes ($p = 0.88$, Wilcoxon signed rank test; $n = 4$ paired recordings, $n = 20$ internodes, 2–6 internodes/OL).
(D) Ca^{2+} event amplitude ($\Delta F/F_0$) was reduced following AP stimulation ($p = 0.018$, Mann-Whitney test). Mean \pm SEM.
(E) Network activity was evoked by reducing extracellular Mg^{2+} to 0.2 mM and blocking inhibition (GABA_A receptor blocker gabazine). OL membrane potentials were temporally synchronized with network burst and exhibited peak depolarizations up to 20 mV. Insets show expanded timescales of ~ 1 s. Scale bars, 10 mV and 1 s.
(F) Boxplot depicting the timing of myelin Ca^{2+} events 3 s before and after network activity compared with randomly generated event times ($p = 0.99$, Kolmogorov-Smirnov test; $n = 4$ OLs). The box indicates 25th and 75th percentiles, the horizontal bar indicates the median, and error bars maximum and minimum.
(G) Left: single-trial Ca^{2+} fluorescence traces overlaid with the average (red trace) before and after increase of network activity. Scale bars, 10% $\Delta F/F_0$ and 0.5 s. Right: summary plot showing Ca^{2+} event frequency before and after increased network activity ($p = 0.88$, Wilcoxon signed rank test; $n = 4$ OLs). Mean \pm SEM.
(H) Single-trial Ca^{2+} fluorescence traces and summary data before and after bath application of TTX ($p = 0.31$, Wilcoxon signed rank test; $n = 6$ OLs). Scale bars, 1 s and 10% $\Delta F/F_0$. Mean \pm SEM.

See also Figure S5.

in MBP-positive internodes from 13 OLs were significantly increased in frequency compared with adult controls (control data: P31–P62 from Figure 2J; $p = 0.0004$, Mann-Whitney test; $n = 12$ OLs; Figures 4D and S4B). The kinetics and amplitude of Ca^{2+} events were similar to those observed during normal early development ($p = 0.18$ and $p = 0.66$, Mann-Whitney test; Figures 4E, S4C, and S4D). One exception was the half-width being longer during remyelination (on average in control: 1.4 ± 0.07 s, $n = 427$ events; remyelination: 1.84 ± 0.16 s, $n = 136$ events; $p = 0.008$, Mann-Whitney test; Figure S4E). Similar to the OL maturation, Ca^{2+} transient frequency was reduced with more depolarized resting membrane potential (Figure S4F). In summary, these data suggest that microdomain Ca^{2+} transients and Ca^{2+} waves in the myelin sheath concur with the active phase of longitudinal and radial myelination.

Microdomain Ca^{2+} Transients in Myelin Are Independent of Neuronal Activity

Are myelin Ca^{2+} events susceptible to neuromodulation? Neuronal activity has been shown to be important for recruitment of OPCs in *de novo* myelination and is linked to Ca^{2+} changes in OPC processes (McKenzie et al., 2014; Wake et al., 2011). We therefore hypothesized that action potential generation may alter the microdomain Ca^{2+} transient frequency or amplitude. To examine this, we simultaneously recorded from a layer 5 pyramidal neuron and the OL ensheathing its first internode (Figure 5A). Simultaneous whole-cell recordings were performed between P18 and P21, the age when myelin segments around the first internode were consistently detected (Figure 1). Myelin Ca^{2+} signals were recorded before and after a train of action potentials (on average ten action potentials at ~ 50 Hz and more than ten

trials). Surprisingly, the results indicated that the frequency of microdomain Ca^{2+} transients was independent of action potential generation in the corresponding axon ($p = 0.73$, Kolmogorov-Smirnov [KS] test; control, $n = 138$; stimulation, $n = 130$ events), and neither affected other internodes of the same OL (Figures 5B and 5C). In fact, the amplitude of microdomain Ca^{2+} transients significantly decreased by $\sim 30\%$ following action potential stimulation (Figure 5D).

Because neocortical OLs myelinate >30 axons, we hypothesized that modulation of myelin Ca^{2+} transients require synchronized network activity. To examine this hypothesis, we experimentally increased neuronal network activity by lowering extracellular Mg^{2+} and partially blocking inhibitory synaptic transmission with $1 \mu\text{M}$ gabazine (a selective GABA_A antagonist). During the network burst, OLs showed highly synchronized depolarizations up to 20.2 ± 2.2 mV from the resting membrane potential ($n = 17$ events from four OLs; Figures 5E and S5A). These depolarizations likely reflect the extracellular K^+ elevations (Battefeld et al., 2016). However, the microdomain Ca^{2+} transients were not temporally related to network bursts, and neither did we observe Ca^{2+} waves (Figure 5F). The Ca^{2+} event frequency, amplitude, and half-width remained similar (Figures 5G and S5B). Finally, blocking voltage-gated Na^+ channels by bath application of TTX provided further evidence that myelin Ca^{2+} events are generated independent from neuronal activity (Figures 5H and S5C). Together, these data suggest that Ca^{2+} events in developing myelin sheaths are either intrinsically generated or require signaling from other glia cells such as astrocytes.

Myelin Ca^{2+} Transients Are Produced by Mitochondria Localized in the Non-compacted Myelin

Which mechanisms produce the myelin Ca^{2+} transients? Previous studies showed that cultured OLs express voltage-gated Ca^{2+} channels and calcium-permeable NMDA receptors, which have been associated with glutamate mediated signaling between neurons and OL lineage cells (Káradóttir et al., 2005; Kirischuk et al., 1995; Micu et al., 2016). Furthermore, second messenger signaling via purinergic G protein-coupled receptors (P2YR) or activation of inositol trisphosphate receptor (IP₃R) or ryanodine receptors (RyRs) is implicated in myelin calcium regulation (James and Butt, 2001; Kirischuk et al., 1995; Micu et al., 2016). Using pharmacological blockers, we tested multiple pathways that could be involved in the generation of myelin Ca^{2+} transients (Figure 6A). Blocking NMDA receptors (DAP-5/MK-801), IP₃R (heparin), and gap junctions (carbenoxolone [CBX]) did not change the frequency, amplitude, and half-width of Ca^{2+} signals (Figures 6B–6D, S6A, and S6B), with the exception being an increased amplitude in the presence of heparin. This robust increase in Ca^{2+} amplitude ($p = 0.026$, Mann-Whitney test; Figure S6A) is potentially a consequence of endoplasmic reticulum (ER) IP₃R block and a successive reduction in intracellular baseline Ca^{2+} level, leading to a larger $\Delta F/F$ amplitude. Moreover, simultaneously blocking IP₃R and RyR with heparin, dantrolene, and ruthenium red did not change myelin Ca^{2+} transient frequency, amplitude, or half-width (Figure S6C). Reducing $[\text{Ca}^{2+}]_0$ to 0.1 mM , however, led to a significant reduction in frequency and amplitude of Ca^{2+} transients in myelin without a change in half-width (Figures

6E, S6A, and S6B), suggesting an ion channel source or an indirect depletion of intracellular Ca^{2+} stores. Both in OPCs and in astrocytes, Ca^{2+} transients and waves are generated by the mitochondrial Ca^{2+} uptake and release from and into the cytosol (Agarwal et al., 2017; Haak et al., 2000, 2002). During periods of high oxidative phosphorylation, the mitochondria membrane depolarizes periodically, releasing Ca^{2+} into the cytosol mediated by the transient opening of the mitochondrial permeability pore (mPTP) (Wang et al., 2008; Ichas et al., 1997). To test the contribution of mitochondria in myelin Ca^{2+} transients, we blocked the mPTP by combining cyclosporin A (inhibiting the cyclophilin D component at the pore) and rotenone (a mitochondrial complex I blocker). Bath application of these mPTP-inhibiting drugs significantly and nearly completely abolished the frequency of Ca^{2+} events ($80 \pm 5\%$ block) in 34 myelin sheaths of 6 oligodendrocytes, while leaving amplitude and event duration of the few remaining Ca^{2+} transients unchanged (Figures 6F, S6A, and S6B). The substantive role of mitochondria is surprising, as their presence within the myelin sheath cytoplasm has only recently been shown at the light and EM level (Rinholm et al., 2016). To determine whether mitochondria are present in myelin sheaths, we examined EM images of P15 and adult mice somatosensory cortex. Despite the small chance of detecting mitochondria in ultrathin EM cross sections of the axon ($\sim 2\%$; Rinholm et al., 2016), in EM images from the P15 mice, we found mitochondria, characterized by at least a few cristae and double outer membrane layer, located within the non-compacted cytoplasmic ridges, including the inner cytoplasmic tongue ($n = 5$) and the paranodal loops ($n = 2$). Similarly, also in the EM from adult mice, mitochondria were observed within the inner cytoplasmic tongue ($n = 8$) and in the cytoplasm of paranodal loops ($n = 2$; Figure 6G). Taken together, these results reveal that a high rate of periodic myelin Ca^{2+} transients is correlated with phases of myelin remodeling and produced by the mitochondria localized to cytoplasmic domains of the myelin sheath.

DISCUSSION

By imaging Ca^{2+} in the mammalian myelin sheath in the deeper layers of the somatosensory cortex at high sensitivity, we observed a highly active period of spontaneous Ca^{2+} events during the first postnatal weeks, characterized by Ca^{2+} signals in small microdomains as well as Ca^{2+} waves propagating along the myelin sheath (Figures 2 and 3). At this age, axonal growth, reorganization, and pruning as well as myelination rapidly develop (Romand et al., 2011; Vincze et al., 2008) (Figure 1). Our approach of filling individual OLs with OGB-1 resulted in high signal-to-noise ratios across experiments, allowing discrimination of Ca^{2+} changes $\geq 5\% \Delta F/F$ (Figures S2B and S2C) and the identification that large-amplitude propagating Ca^{2+} waves (Figure 2) are built up by a brief burst of multiple Ca^{2+} transients ($\sim 0.8 \text{ Hz}$), suggesting that they share a common source. These findings are in good agreement with recent work linking myelin Ca^{2+} events with growth and disassembly of the myelin sheath in zebrafish during the early stages of myelination (Baraban et al., 2018; Krasnow et al., 2018). In contrast, we observed Ca^{2+} events at a remarkably high rate of $\sim 0.2 \text{ Hz}$ (Figures 2F

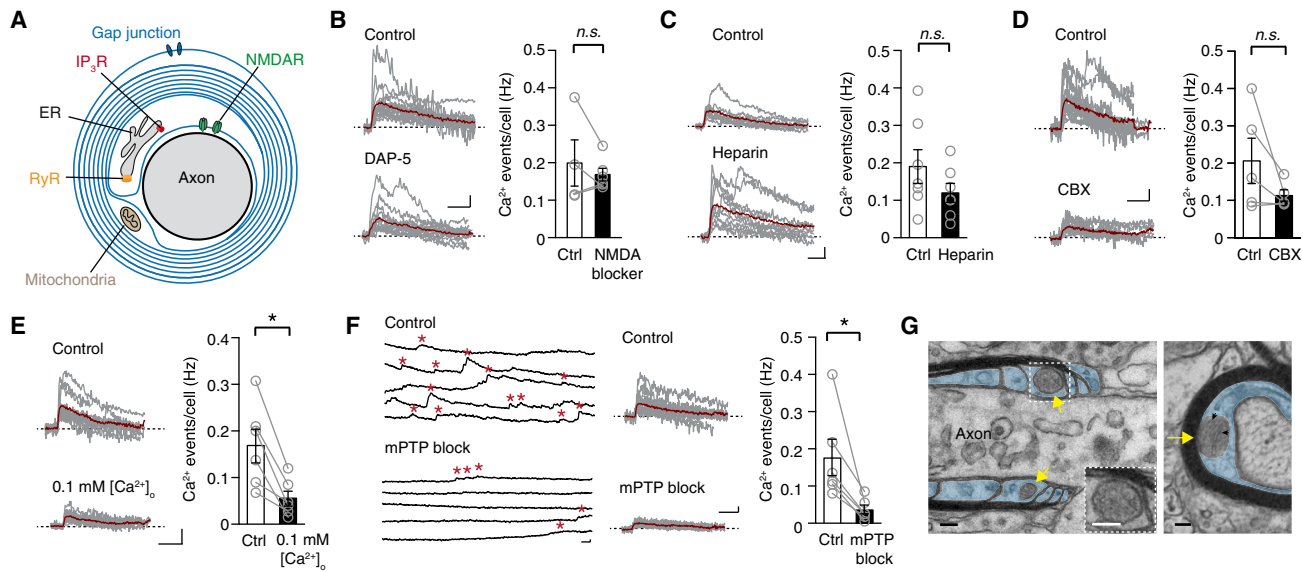


Figure 6. Myelin Microdomain Ca²⁺ Transients Are Generated by Mitochondria in Non-compacted Myelin

(A) Schematic overview of putative receptors and pathways implicated in myelin Ca²⁺. Ca²⁺ entry could be triggered by activation of NMDA receptors (NMDAR), downstream activation of intracellular IP₃R or ryanodine receptor (RyR), gap-junction coupling with astrocytes or mitochondria.

(B) Example traces and pooled summary data for paired DAP-5 wash-in experiments (connecting lines) and intracellular application of MK-801 (single data points). No effect of NMDA receptor block on event frequency was observed ($p = 0.91$, Mann-Whitney test; ctrl: $n = 4$ OLs, NMDA block = 6 OLs). Mean \pm SEM.

(C) Example traces and summary plot for Ca²⁺ event frequency for control and intracellular IP₃R block by heparin shows no change ($p = 0.21$, Mann-Whitney test; $n = 7$ OLs for each condition). Mean \pm SEM.

(D) Examples traces and summary plots for the effect of gap-junction blocker carbenoxolone ($p = 0.18$, Wilcoxon-signed rank test; $n = 5$ OLs). Mean \pm SEM.

(E) Reduction of extracellular [Ca²⁺] to 0.1 mM reduces Ca²⁺ event frequency in myelin ($p = 0.03$, Wilcoxon-signed rank test; $n = 6$ OLs). Mean \pm SEM.

(F) Left: example traces showing 5 \times 20 s of myelin Ca²⁺ imaging in control and after inhibition of the mitochondrial permeability transition pore (mPTP) with 20 μ M cyclosporine A and 10 μ M rotenone. Asterisks indicate Ca²⁺ transients. Middle and right: individual Ca²⁺ events (gray) and average Ca²⁺ event frequency (red) showing a significant reduction following mPTP block ($p = 0.03$, Wilcoxon-signed rank test; $n = 34$ internodes from 6 OLs). Scale bars for all imaging traces from (B) to (F), 1 s and 10% $\Delta F/F_0$. Mean \pm SEM.

(G) Left: example EM image mitochondria (yellow arrows) in the cytoplasm of paranodal myelin (false blue colored) in the adult somatosensory cortex. Right: EM image of a mitochondrion located in the inner cytoplasmic loop, the adaxonal myelin. Note the presence of cristae within the mitochondrion (black arrowheads). Scale bars, 100 nm.

See also Figure S6.

and 3B), two orders of magnitude higher than those in zebrafish ($\sim 1\text{--}2$ mHz in (Baraban et al., 2018; Krasnow et al., 2018). The discrepancy could be due to technical differences in acquiring Ca²⁺ signals (*in vivo* two-photon and confocal microscopy versus *in vitro* one-photon epifluorescence imaging in the present study) or the different kinetics of genetic versus synthetic Ca²⁺ reporters. It is equally possible that the Ca²⁺ events reported in zebrafish myelin (Baraban et al., 2018; Krasnow et al., 2018) imaged over longer time periods and low acquisition rates (~ 0.4 Hz) are actually Ca²⁺ waves. Indeed, Ca²⁺ waves typically occur at a low rate of ~ 0.2 events/min and have a relatively long half-width duration of ~ 10 s (Figure 2).

Unexpectedly, we did not find evidence that neuronal activity drives oligodendroglial Ca²⁺ (Figure 5). Axonal vesicle release during neuronal activity in zebrafish initiates and stabilizes myelin segments during their transition from OPC to OL (Hines et al., 2015; Mensch et al., 2015; Wake et al., 2011), and extracellular axonal stimulation of the spinal cord doubles the rate of Ca²⁺ events in segments of developing OLs (Krasnow et al., 2018). In addition to the technical differences between the studies as mentioned above, we cannot exclude that the discrepancy

stems from the distinct developmental stages of OLs (3–4 days post-fertilization in zebrafish versus 13–56 postnatal days in mice), interspecies differences, or OL cell-type differences between neuronal circuits. In support of the latter argument, myelination of commissural primary ascending axons in zebrafish spinal cord forms independently of vesicle release, whereas myelin ensheathment of reticulospinal axons is regulated by activity-dependent vesicle release (Koudelka et al., 2016). Mammalian OLs consist of six genetically distinct subpopulations of mature OLs, two types of which are found primarily in the somatosensory cortex and corpus callosum (Marques et al., 2016). Recent work shows that the auditory brain stem contains a large fraction of pre-myelinating OL types, of which some express Na⁺ channels, and in this brain region myelination is increased by neuronal activity (Berret et al., 2017). Whether myelin Ca²⁺ activity differs between OL populations and how these are linked with differential activity dependence of myelination remains to be established.

The high rate of microdomain Ca²⁺ transients permitted a controlled pharmacological characterization revealing that inhibition of the transient opening of the mitochondrial mPTP selectively and nearly completely abolished Ca²⁺ events in myelin

sheaths (Figure 6). These findings are in good agreement with previous studies in OPCs and myelin-like processes in cultured oligodendrocytes, which identified a major role of mitochondria in producing Ca^{2+} transients and facilitating Ca^{2+} wave propagation (Haak et al., 2002; 2000; Simpson and Russell, 1996). In addition to the substantial impact of the mitochondrial inhibitors, we discovered that myelin in the neocortex does contain mitochondria organelles located in the cytoplasmic ridges of the sheath, including the adaxonal myelin and paranodal loops (Figure 6). These results are in support of the recently identified small and sparsely moving atypical mitochondria identified in cytoplasm of OLs (Rinholm et al., 2016). During periods of high respiration, mPTPs undergo periods of quantal low-conductance openings, leading to a resetting of the mitochondrial membrane potentials, transient efflux of Ca^{2+} from the mitochondria into the cytosol, and the continuation of ATP production (Ichas et al., 1997; Wang et al., 2008). Indeed, in OPCs and thin processes of astrocytes, a strong anatomical overlap was observed between mitochondrial locations and Ca^{2+} microdomains (Agarwal et al., 2017; Haak et al., 2000; Simpson and Russell, 1996). Interestingly, in myelin sheaths, we did not observe a contribution of ER Ca^{2+} release from IP₃ or RyRs (Figures 6 and S6). Our findings resemble the spontaneous Ca^{2+} transients in astrocytic processes, which are generated by mPTP opening and persist in the absence of IP₃ receptors (Agarwal et al., 2017; Srinivasan et al., 2015). One caveat of our approach is the rare occurrence of Ca^{2+} waves during typical patch-clamp recording experiments, which prohibited the investigation of the nature of the waves or their dependence on neuronal activity. To examine whether ER Ca^{2+} is critical for producing Ca^{2+} waves future experiments would require other means, such as, for example, the sparse expression of genetically encoded Ca^{2+} indicators, enabling *in vivo* and long-term imaging.

What could be the role of autonomous transient Ca^{2+} release by mitochondria in the myelin sheath? A downstream target of Ca^{2+} could be the recruitment of Ca^{2+} /calmodulin-dependent kinase inducing MBP membrane binding via phosphatidylinositol 4,5-bisphosphate (PIP₂), or actin disassembly to induce oligodendroglial membrane wrapping (Nawaz et al., 2009, 2015; Waggner et al., 2013; Zuchero et al., 2015). Although the biophysical axon-glia signaling pathways that match myelin sheath thickness to axon diameter remain to be identified (Chang et al., 2016), we speculate that in the deeper layers of the somatosensory cortex, axon diameter may suffice as an instructive signal for myelination. It has been estimated that rat oligodendrocytes may produce up to $\sim 5,000 \mu\text{m}^2$ of myelin membrane per day or 10^5 myelin proteins per minute (Pfeiffer et al., 1993). In this view, the high frequency of Ca^{2+} events ensures a high respiratory rate and mitochondrial ATP production (Ichas et al., 1997) for lipid trafficking and myelin biosynthesis (Voelker, 1984). Such a cell-autonomous signaling pathway is in good agreement with the notion that biosynthesis of the proteins and lipids for the myelin sheaths occurs largely in the absence of neurons (Nawaz et al., 2015; Rosenberg et al., 2008). Furthermore, cultured OLs ensheathe synthetic nanofibers greater than $\sim 0.4 \mu\text{m}$ in diameter, suggesting that the molecular or biophysical mechanisms of axon selection and initiation of spiral myelin wrapping are intrinsic to the OL (Lee

et al., 2012). In future studies, it will be interesting to address the interplay of molecular pathways regulating membrane growth and the signaling mechanisms regulating mitochondria respiration and myelin lipid production. Mitochondria-generated cytoplasmic Ca^{2+} may support coordination of myelin sheath remodeling at the inner tongue and paranodes, allowing the lateral movement of cytoplasmic loops and refinement of the organization of myelinated axons toward the nodes of Ranvier (Snaidero et al., 2014). One hypothesis emerging from the present data is that spatially distributed waves of high $[\text{Ca}^{2+}]_i$ mediate actin disassembly, thereby providing the driving force for advancing the spiral wrapping of the lamellae (Baraban et al., 2018; Nawaz et al., 2015; Zuchero et al., 2015), while small $[\text{Ca}^{2+}]_i$ changes evoked during microdomain Ca^{2+} transients stabilize the myelin sheath and mediate compaction and myelin sheath refinement. To further resolve the relationship between myelin Ca^{2+} activity and myelination patterns, longitudinal time-lapse *in vivo* studies simultaneously monitoring activity and cortical myelination would be required.

In summary, our study uncovered a remarkably high rate of mitochondria-dependent local Ca^{2+} transients and Ca^{2+} waves propagating along the mammalian myelin sheath during myelin remodeling, providing biochemical and cellular insights into the mechanism of *de novo* myelin formation and remyelination in neocortical circuits.

STAR★METHODS

Detailed methods are provided in the online version of this paper and include the following:

- KEY RESOURCES TABLE
- CONTACT FOR REAGENT AND RESOURCE SHARING
- EXPERIMENTAL MODEL AND SUBJECT DETAILS
 - Mice
- METHOD DETAILS
 - Brain slice preparation
 - Electrophysiology
 - Epifluorescence calcium imaging of oligodendrocytes
 - Ratiometric fura-2 Ca^{2+} imaging
 - Immunohistochemistry
 - EM
- QUANTIFICATION AND STATISTICAL ANALYSIS
 - Analysis of Ca^{2+} imaging data
 - Calculation of free $[\text{Ca}^{2+}]_i$
 - Analysis of myelin distribution and g-ratio
 - Morphological reconstructions
 - Statistical tests
- DATA AND SOFTWARE AVAILABILITY

SUPPLEMENTAL INFORMATION

Supplemental Information includes six figures and two videos and can be found with this article online at <https://doi.org/10.1016/j.celrep.2018.12.039>.

ACKNOWLEDGMENTS

We thank the members of the Axonal Signaling Group (NIN) for helpful discussion and critical reading of the manuscript. This research was supported

by the European Research Council (ERC StG 261114), Hersenstichting Nederland (grant 2013[1]-160), and the National Multiple Sclerosis Society (RG 4924A1/1).

AUTHOR CONTRIBUTIONS

Conceptualization, A.B. and M.H.P.K.; Methodology, A.B., M.A.P., and M.H.P.K.; Investigation, A.B. and S.I.V.; Software, M.A.P.; Interpretation of Data, A.B., M.A.P., and M.H.P.K.; Writing – Original Draft, A.B.; Writing – Review & Editing, A.B. and M.H.P.K., with input from M.A.P. and S.I.V.; Funding Acquisition, M.H.P.K. All authors approved the final version of the manuscript.

DECLARATION OF INTEREST

The authors declare no competing interests.

Received: May 21, 2018

Revised: November 9, 2018

Accepted: December 7, 2018

Published: January 2, 2019

REFERENCES

- Agarwal, A., Wu, P.-H., Hughes, E.G., Fukaya, M., Tischfield, M.A., Langseth, A.J., Wirtz, D., and Bergles, D.E. (2017). Transient opening of the mitochondrial permeability transition pore induces microdomain calcium transients in astrocyte processes. *Neuron* 93, 587–605.e7.
- Baraban, M., Koudelka, S., and Lyons, D.A. (2018). Ca²⁺ activity signatures of myelin sheath formation and growth in vivo. *Nat. Neurosci.* 21, 19–23.
- Barres, B.A., and Raff, M.C. (1999). Axonal control of oligodendrocyte development. *J. Cell Biol.* 147, 1123–1128.
- Battefeld, A., Klooster, J., and Kole, M.H.P. (2016). Myelinating satellite oligodendrocytes are integrated in a glial syncytium constraining neuronal high-frequency activity. *Nat. Commun.* 7, 11298.
- Baxi, E.G., DeBruin, J., Jin, J., Strasburger, H.J., Smith, M.D., Orthmann-Murphy, J.L., Schott, J.T., Fairchild, A.N., Bergles, D.E., and Calabresi, P.A. (2017). Lineage tracing reveals dynamic changes in oligodendrocyte precursor cells following cuprizone-induced demyelination. *Glia* 65, 2087–2098.
- Berret, E., Barron, T., Xu, J., Debner, E., Kim, E.J., and Kim, J.H. (2017). Oligodendroglial excitability mediated by glutamatergic inputs and Nav1.2 activation. *Nat. Commun.* 8, 557.
- Chang, K.-J., Redmond, S.A., and Chan, J.R. (2016). Remodeling myelination: implications for mechanisms of neural plasticity. *Nat. Neurosci.* 19, 190–197.
- Clarmer, T., Diederichs, F., Berger, K., Denecke, B., Gan, L., van der Valk, P., Beyer, C., Amor, S., and Kipp, M. (2012). Myelin debris regulates inflammatory responses in an experimental demyelination animal model and multiple sclerosis lesions. *Glia* 60, 1468–1480.
- Fard, M.K., van der Meer, F., Sánchez, P., Cantuti-Castelvetri, L., Mandad, S., Jäkel, S., Fornasiero, E.F., Schmitt, S., Ehrlich, M., Starost, L., et al. (2017). BCAS1 expression defines a population of early myelinating oligodendrocytes in multiple sclerosis lesions. *Sci. Transl. Med.* 9, eaam7816.
- Friess, M., Hammann, J., Unichenko, P., Luhmann, H.J., White, R., and Kirischuk, S. (2016). Intracellular ion signaling influences myelin basic protein synthesis in oligodendrocyte precursor cells. *Cell Calcium* 60, 322–330.
- Grynkiewicz, G., Poenie, M., and Tsien, R.Y. (1985). A new generation of Ca²⁺ indicators with greatly improved fluorescence properties. *J. Biol. Chem.* 260, 3440–3450.
- Haak, L.L., Grimaldi, M., and Russell, J.T. (2000). Mitochondria in myelinating cells: calcium signaling in oligodendrocyte precursor cells. *Cell Calcium* 28, 297–306.
- Haak, L.L., Grimaldi, M., Smaili, S.S., and Russell, J.T. (2002). Mitochondria regulate Ca²⁺ wave initiation and inositol trisphosphate signal transduction in oligodendrocyte progenitors. *J. Neurochem.* 80, 405–415.
- Hamada, M.S., and Kole, M.H.P. (2015). Myelin loss and axonal ion channel adaptations associated with gray matter neuronal hyperexcitability. *J. Neurosci.* 35, 7272–7286.
- Helmchen, F., Imoto, K., and Sakmann, B. (1996). Ca²⁺ buffering and action potential-evoked Ca²⁺ signaling in dendrites of pyramidal neurons. *Biophys. J.* 70, 1069–1081.
- Hill, R.A., Li, A.M., and Grutzendler, J. (2018). Lifelong cortical myelin plasticity and age-related degeneration in the live mammalian brain. *Nat. Neurosci.* 21, 683–695.
- Hines, M.L., and Carnevale, N.T. (2001). NEURON: a tool for neuroscientists. *Neuroscientist* 7, 123–135.
- Hines, J.H., Ravanelli, A.M., Schwindt, R., Scott, E.K., and Appel, B. (2015). Neuronal activity biases axon selection for myelination in vivo. *Nat. Neurosci.* 18, 683–689.
- Hirrlinger, P.G., Scheller, A., Braun, C., Quintela-Schneider, M., Fuss, B., Hirrlinger, J., and Kirchhoff, F. (2005). Expression of reef coral fluorescent proteins in the central nervous system of transgenic mice. *Mol. Cell. Neurosci.* 30, 291–303.
- Hughes, E.G., Orthmann-Murphy, J.L., Langseth, A.J., and Bergles, D.E. (2018). Myelin remodeling through experience-dependent oligodendrogenesis in the adult somatosensory cortex. *Nat. Neurosci.* 21, 696–706.
- Ichas, F., Jouaville, L.S., and Mazat, J.P. (1997). Mitochondria are excitable organelles capable of generating and conveying electrical and calcium signals. *Cell* 89, 1145–1153.
- James, G., and Butt, A.M. (2001). P2X and P2Y purinoreceptors mediate ATP-evoked calcium signalling in optic nerve glia in situ. *Cell Calcium* 30, 251–259.
- Káradóttir, R., Cavelier, P., Bergersen, L.H., and Attwell, D. (2005). NMDA receptors are expressed in oligodendrocytes and activated in ischaemia. *Nature* 438, 1162–1166.
- Kirischuk, S., Scherer, J., Kettenmann, H., and Verkhratsky, A. (1995). Activation of P₂-purinoreceptors triggered Ca²⁺ release from InsP₃-sensitive internal stores in mammalian oligodendrocytes. *J. Physiol.* 483, 41–57.
- Koudelka, S., Voas, M.G., Almeida, R.G., Baraban, M., Soetaert, J., Meyer, M.P., Talbot, W.S., and Lyons, D.A. (2016). Individual neuronal subtypes exhibit diversity in CNS myelination mediated by synaptic vesicle release. *Curr. Biol.* 26, 1447–1455.
- Krasnow, A.M., Ford, M.C., Valdivia, L.E., Wilson, S.W., and Attwell, D. (2018). Regulation of developing myelin sheath elongation by oligodendrocyte calcium transients in vivo. *Nat. Neurosci.* 21, 24–28.
- Kukley, M., Capetillo-Zarate, E., and Dietrich, D. (2007). Vesicular glutamate release from axons in white matter. *Nat. Neurosci.* 10, 311–320.
- Lee, S., Leach, M.K., Redmond, S.A., Chong, S.Y.C., Mellon, S.H., Tuck, S.J., Feng, Z.-Q., Corey, J.M., and Chan, J.R. (2012). A culture system to study oligodendrocyte myelination processes using engineered nanofibers. *Nat. Methods* 9, 917–922.
- Marques, S., Zeisel, A., Codeluppi, S., van Bruggen, D., Mendanha Falcão, A., Xiao, L., Li, H., Häring, M., Hochgerner, H., Romanov, R.A., et al. (2016). Oligodendrocyte heterogeneity in the mouse juvenile and adult central nervous system. *Science* 352, 1326–1329.
- McKenzie, I.A., Ohayon, D., Li, H., de Faria, J.P., Emery, B., Tohyama, K., and Richardson, W.D. (2014). Motor skill learning requires active central myelination. *Science* 346, 318–322.
- Mensch, S., Baraban, M., Almeida, R., Czopka, T., Ausborn, J., El Manira, A., and Lyons, D.A. (2015). Synaptic vesicle release regulates myelin sheath number of individual oligodendrocytes in vivo. *Nat. Neurosci.* 18, 628–630.
- Micu, I., Plemel, J.R., Lachance, C., Proft, J., Jansen, A.J., Cummins, K., van Minnen, J., and Stys, P.K. (2016). The molecular physiology of the axo-myelinic synapse. *Exp. Neurol.* 276, 41–50.
- Miyazaki, K., and Ross, W.N. (2015). Simultaneous sodium and calcium imaging from dendrites and axons. *eNeuro* 2, ENEURO.0092-15.2015.

- Myatt, D.R., Hadlington, T., Ascoli, G.A., and Nasuto, S.J. (2012). Neuromantic - from semi-manual to semi-automatic reconstruction of neuron morphology. *Front. Neuroinform.* 6, 4.
- Nave, K.-A., and Werner, H.B. (2014). Myelination of the nervous system: mechanisms and functions. *Annu. Rev. Cell Dev. Biol.* 30, 503–533.
- Nawaz, S., Kippert, A., Saab, A.S., Werner, H.B., Lang, T., Nave, K.-A., and Simons, M. (2009). Phosphatidylinositol 4,5-bisphosphate-dependent interaction of myelin basic protein with the plasma membrane in oligodendroglial cells and its rapid perturbation by elevated calcium. *J. Neurosci.* 29, 4794–4807.
- Nawaz, S., Sánchez, P., Schmitt, S., Snaidero, N., Mitkovski, M., Velte, C., Brückner, B.R., Alexopoulos, I., Czopka, T., Jung, S.Y., et al. (2015). Actin filament turnover drives leading edge growth during myelin sheath formation in the central nervous system. *Dev. Cell* 34, 139–151.
- Nishiyama, A., Komitova, M., Suzuki, R., and Zhu, X. (2009). Polydendrocytes (NG2 cells): multifunctional cells with lineage plasticity. *Nat. Rev. Neurosci.* 10, 9–22.
- Pfeiffer, S.E., Warrington, A.E., and Bansal, R. (1993). The oligodendrocyte and its many cellular processes. *Trends Cell Biol.* 3, 191–197.
- Rinholm, J.E., Vervaeke, K., Tadross, M.R., Tkachuk, A.N., Kopek, B.G., Brown, T.A., Bergersen, L.H., and Clayton, D.A. (2016). Movement and structure of mitochondria in oligodendrocytes and their myelin sheaths. *Glia* 64, 810–825.
- Romand, S., Wang, Y., Toledo-Rodriguez, M., and Markram, H. (2011). Morphological development of thick-tufted layer V pyramidal cells in the rat somatosensory cortex. *Front. Neuroanat.* 5, 5.
- Rosenberg, S.S., Kelland, E.E., Tokar, E., De la Torre, A.R., and Chan, J.R. (2008). The geometric and spatial constraints of the microenvironment induce oligodendrocyte differentiation. *Proc. Natl. Acad. Sci. U.S.A.* 105, 14662–14667.
- Schindelin, J., Arganda-Carreras, I., Frise, E., Kaynig, V., Longair, M., Pietzsch, T., Preibisch, S., Rueden, C., Saalfeld, S., Schmid, B., et al. (2012). Fiji: an open-source platform for biological-image analysis. *Nat. Methods* 9, 676–682.
- Schoenmakers, T.J., Visser, G.J., Flik, G., and Thevenet, A.P. (1992). CHELATOR: an improved method for computing metal ion concentrations in physiological solutions. *Biotechniques* 12, 870–879.
- Simpson, P.B., and Russell, J.T. (1996). Mitochondria support inositol 1,4,5-trisphosphate-mediated Ca^{2+} waves in cultured oligodendrocytes. *J. Biol. Chem.* 271, 33493–33501.
- Snaidero, N., Möbius, W., Czopka, T., Hekking, L.H.P., Mathisen, C., Verkleij, D., Goebels, S., Edgar, J., Merkler, D., Lyons, D.A., et al. (2014). Myelin membrane wrapping of CNS axons by PI(3,4,5)P3-dependent polarized growth at the inner tongue. *Cell* 156, 277–290.
- Srinivasan, R., Huang, B.S., Venugopal, S., Johnston, A.D., Chai, H., Zeng, H., Golshani, P., and Khakh, B.S. (2015). Ca^{2+} signaling in astrocytes from $\text{Ip3r2}^{-/-}$ mice in brain slices and during startle responses *in vivo*. *Nat. Neurosci.* 18, 708–717.
- Stevens, B., Porta, S., Haak, L.L., Gallo, V., and Fields, R.D. (2002). Adenosine: a neuron-glial transmitter promoting myelination in the CNS in response to action potentials. *Neuron* 36, 855–868.
- Sun, W., Matthews, E.A., Nicolas, V., Schoch, S., and Dietrich, D. (2016). NG2 glial cells integrate synaptic input in global and dendritic calcium signals. *eLife* 5, e16262.
- Vincze, A., Mázló, M., Seress, L., Komoly, S., and Abrahám, H. (2008). A correlative light and electron microscopic study of postnatal myelination in the murine corpus callosum. *Int. J. Dev. Neurosci.* 26, 575–584.
- Voelker, D.R. (1984). Phosphatidylserine functions as the major precursor of phosphatidylethanolamine in cultured BHK-21 cells. *Proc. Natl. Acad. Sci. U.S.A.* 81, 2669–2673.
- Waggner, C.T., Dupree, J.L., Elgersma, Y., and Fuss, B. (2013). CaMKII β regulates oligodendrocyte maturation and CNS myelination. *J. Neurosci.* 33, 10453–10458.
- Wake, H., Lee, P.R., and Fields, R.D. (2011). Control of local protein synthesis and initial events in myelination by action potentials. *Science* 333, 1647–1651.
- Wang, W., Fang, H., Groom, L., Cheng, A., Zhang, W., Liu, J., Wang, X., Li, K., Han, P., Zheng, M., et al. (2008). Superoxide flashes in single mitochondria. *Cell* 134, 279–290.
- Yoo, A.S., Krieger, C., and Kim, S.U. (1999). Process extension and intracellular Ca^{2+} in cultured murine oligodendrocytes. *Brain Res.* 827, 19–27.
- Young, K.M., Psachoulia, K., Tripathi, R.B., Dunn, S.-J., Cossell, L., Attwell, D., Tohyama, K., and Richardson, W.D. (2013). Oligodendrocyte dynamics in the healthy adult CNS: evidence for myelin remodeling. *Neuron* 77, 873–885.
- Zhang, Y., Chen, K., Sloan, S.A., Bennett, M.L., Scholze, A.R., O'Keeffe, S., Phatnani, H.P., Guarnieri, P., Caneda, C., Ruderisch, N., et al. (2014). An RNA-sequencing transcriptome and splicing database of glia, neurons, and vascular cells of the cerebral cortex. *J. Neurosci.* 34, 11929–11947.
- Zuchero, J.B., Fu, M.-M., Sloan, S.A., Ibrahim, A., Olson, A., Zaremba, A., Dugas, J.C., Wienbar, S., Caprariello, A.V., Kantor, C., et al. (2015). CNS myelin wrapping is driven by actin disassembly. *Dev. Cell* 34, 152–167.

STAR★METHODS

KEY RESOURCES TABLE

REAGENT or RESOURCE	SOURCE	IDENTIFIER
Antibodies		
Mouse anti myelin myelin oligodendrocyte glycoprotein (MOG, 1:1000)	Millipore	Cat#: MAB5680; RRID: AB_1587278
Chicken anti proteo-lipid-protein (PLP, 1:250)	Millipore	Cat#: Ab15454; RRID: AB_805413
Rabbit anti myelin basic protein (MBP, 1:250)	Millipore	Cat#: AB980; RRID: AB_92396
Rabbit - anti-GFP (1:1500)	Abcam	Cat#: ab6556; RRID: AB_305564
Alexa488 - Streptavidin (1:500)	Thermofisher	Cat#: S32354; RRID: AB_2336881
Alexa555 - Streptavidin (1:500)	Thermofisher	Cate#: S21381; RRID: AB_2307336
Alexa594 - Streptavidin (1:500)	Thermofisher	Cat#: S11227; RRID: AB_2313574
Chemicals, Peptides, and Recombinant Proteins		
Cuprizone	Sigma-Aldrich	Cat#: C9012
Oregon Green BAPTA-1 hexapotassium salt	Thermo-Fisher	Cat#: O6806
Fura-2	Thermo-Fisher	Cat#: F1200
Biocytin	Sigma	Cat#: B4261
Tetrodotoxin (TTX) citrate	Tocris	Cat#: 1069/1
D-AP5	Tocris	Cat#: 0106/1
Carbenoxolone	Sigma-Aldrich	Cat#: C4790
Gabazine (SR-95531)	Sigma-Aldrich	Cat#: S106
Heparin	Tocris	Cat#: 2812/100
Ruthenium Red	Tocris	Cat#: 1439/100
Dantrolene	Tocris	Cat#: 0507/100
Rotenone	Tocris	Cat#: 3616/50
Cyclosporin A	Tocris	Cat#: 1101/100
Experimental Models: Organisms/Strains		
Mouse: PLP-ECFP (line Q)	Frank Kirchhoff	(Battefeld et al., 2016 ; Hirrlinger et al., 2005)
Mouse: C57BL6/J	The Jackson Laboratory	Cat#: 000664
Oligonucleotides		
FW sequencing primers for PLP-PCFQ: 5'-ATGCGTACCTGACTTCTCCTCT-3'	(Battefeld et al., 2016)	(Hirrlinger et al., 2005)
RV sequencing primers for PLP-PCFQ: 5'-ACTGGGTGCTCAG GTACTGGTTGT-3'	(Battefeld et al., 2016)	(Hirrlinger et al., 2005)
Software and Algorithms		
NeuroPlex	RedShirt Imaging	RRID: SCR_016193
Axograph X	Axograph	RRID: SCR_014284
Graph Pad Prism	GraphPad	RRID: SCR_002798
FIJI	(Schindelin et al., 2012)	RRID: SCR_002285
Neuromantic	(Myatt et al., 2012)	RRID: SCR_013597
NEURON	(Hines and Carnevale, 2001)	RRID: SCR_005393
Maxchelator	(Schoenmakers et al., 1992)	RRID: SCR_000459
Frame splitter	This paper	https://github.com/Kolelab/Image-analysis
ΔF/F calculator	This paper	https://github.com/Kolelab/Image-analysis
Other		
Vibratome	Leica	VT1200
Upright microscope	Olympus	BX61WI
Blue LED 470 nm	Thorlabs	M470L3

(Continued on next page)

Continued

REAGENT or RESOURCE	SOURCE	IDENTIFIER
UV LED 340 nm	Thorlabs	M340L4
Violet LED 420 nm	Thorlabs	M420L3 (discontinued)
NeuroCCD-SMQ camera	RedShirt	N/A

CONTACT FOR REAGENT AND RESOURCE SHARING

Further information and requests for resources and reagents should be directed to and will be fulfilled by the Lead Contact, Maarten Kole (m.kole@nin.knaw.nl).

EXPERIMENTAL MODEL AND SUBJECT DETAILS**Mice**

All procedures involving experimental animals were in agreement with EU directive 2010/63/EU and Dutch law and were approved by the local animal ethics committee of the Royal Netherlands Academy of Arts and Sciences (NIN 12.67, NIN11.70). We used male and female mice of either the C57BL/6 strain or the transgenic PLP-ECFP strain (line Q, as previously described (Battefeld et al., 2016) – obtained from Frank Kirchhoff, University of Saarland, Germany) that were kept on a C57BL/6 background. All transgenic mice were bred in house in a SPF facility, kept on a 12/12 hour light/dark cycle and had access to *ad libitum* standard chow and water. Male mice were randomly assigned to experimentally induced demyelination. Demyelination was induced by feeding mice with 0.2% cuprizone (C9012, Sigma-Aldrich Chemie N.V., Zwijndrecht, the Netherlands) supplemented to the standard diet for 5 weeks (Hamada and Kole, 2015). The standard chow was ground before being mixed with fresh cuprizone and replaced every 2-3 days. Following the 5 weeks treatment, mice were put back on normal chow diet for 1 to 5 weeks to allow remyelination.

METHOD DETAILS**Brain slice preparation**

For all experiments acute slices were prepared from male (61 out of 93) or female (32 out of 93) mice between postnatal day 8 (P8) and P111 in the morning. Mice were anesthetized with 3% isoflurane inhalation, decapitated and the brain was quickly removed and placed in ice-cold ACSF (in mM: 125 NaCl, 25 NaHCO₃, 1.25 NaH₂PO₄, 3 KCl, 25 glucose, 1 CaCl₂, 6 MgCl₂ and 1 kynurenic acid) saturated with 95% O₂ and 5% CO₂. Subsequently we prepared 300 - 400 µm thick parasagittal slices with a vibratome (VT1200S, Leica Microsystems, Germany) and incubated at 35°C for 35 min. Afterward slices were stored in the same solution at room temperature for the experimental day.

Electrophysiology

For physiology experiments slices were transferred to a submerged recording chamber mounted on an upright microscope (BX61WI, Olympus) perfused with ACSF (in mM: 125 NaCl, 25 NaHCO₃, 1.25 NaH₂PO₄, 3 KCl, 25 glucose, 2 CaCl₂, 1 MgCl₂) heated to 33 ± 2°C. Cells were visualized with oblique contrast and OLs were identified by their ECFP fluorescence using a standard filter cube (U-MCFPHQ, Olympus). For whole-cell recordings the intracellular solution consisted of (in mM): 130 K-Gluconate, 10 KCl, 10 HEPES, 4 Mg-ATP, 0.3 Na₂-GTP, 10 Na₂-phosphocreatine and pH set to 7.25 (~280 mOsm). This solution was supplemented with 100 µM of the fluorescent Ca²⁺ indicator Oregon Green BAPTA-1 hexapotassium (OGB-1, O6806, Thermo Fisher Scientific, Landsmeer, Netherlands) for Ca²⁺ imaging experiments (for details see *epifluorescence calcium imaging*). For some experiments, we included 5 mg/ml biocytin (Sigma) for post hoc morphology analysis. The intracellular solution for neurons in paired neuron-oligodendrocyte recordings was supplemented with 75-100 µM Alexa-594-hydrazide (Thermo Fisher Scientific) to identify myelin-axon assemblies. Voltage-clamp and current-clamp recordings were made with Axopatch 200B (Molecular Devices, Sunnyvale, CA, USA) and BVC-700A amplifiers (Dagan Corporation, Minneapolis, MN, USA), respectively. Current or voltage signals were digitized with an AD board (ITC-18, HEKA Elektronik, Lambrecht, Germany) and Axograph X software (RRID: SCR_014284, v1.3.5, Axograph Scientific, Sydney, Australia). Recordings were analog filtered at 10 kHz (Bessel) before digitizing with a minimum of 20 kHz.

Epifluorescence calcium imaging of oligodendrocytes

Oligodendrocyte cell bodies were identified using the ECFP signal which also allows imaging [Ca²⁺] with blue light, enabling the use of the high-affinity Ca²⁺ reporter OGB-1 with minimal fluorescence crosstalk. Epifluorescence Ca²⁺ imaging was performed on a BX61WI microscope (Olympus, Leiderdorp, the Netherlands) with a 60 × 1.0 NA water immersion objective. A blue LED (peak 470 nm, Thorlabs Inc, Newton NJ, USA) equipped with a band pass excitation filter (460-490 nm, Olympus) was used as fluorescence light source and coupled into the light path via a U-DP and U-DPXC1 adaptor (Olympus). Excitation light was reflected with a beam splitter (FF510-Di02, Semrock, Rochester, NY, USA) and emission was band pass (536/40-25, Semrock) or long pass

(FGL515, Thorlabs) filtered before being projected to a NeuroCCD camera (RedShirtImaging LLC, Decatur, GA, USA). The camera has a low spatial resolution of 80×80 pixels, but low read noise and a high dynamic range. To fully illuminate the imaging chip, the camera was mounted on a $0.35 \times$ or $0.38 \times$ de-magnifier tube, resulting in a pixel size of 0.92 or $0.95 \mu\text{m}$, respectively. Oligodendrocytes were loaded with OGB-1 for a minimum of 45 minutes before starting image acquisition that was performed with Neuroplex software (RRID: SCR_016193, v. 10.1.2, RedShirt Imaging) with a sampling frequency of 40 Hz and the camera gain set to 30. Using TTL synchronization, imaging and electrophysiological recording start times were matched. Usually, 10 to 20 trials with a duration of 10 or 20 s were collected for a given field of view. The imaged area was selected to obtain a focal image of a single or several internodes, located some distance from the cell body. Illumination of the field of view was restricted by a field stop with a variable iris that was mounted into the excitation light path. Using this approach the soma, pipette and other unwanted processes (including gap-junction coupled astrocytes) were not illuminated and the dynamic range was increased. The OL resting membrane potential was continuously monitored and depolarizations > 10 mV from the resting membrane potential led to abortion of the experiments and data were excluded from the analyses. In 95% of recordings the same internodes were imaged for control and drug condition. Drugs [$1 \mu\text{M}$ TTX (5 ± 0.5 minutes), $50 \mu\text{M}$ DAP-5 (14 ± 5), $100 \mu\text{M}$ carbenoxolone (14 ± 2 minutes), and $1 \mu\text{M}$ gabazine (9 ± 2 minutes)] were washed in after control Ca^{2+} signals were collected with the exception of intracellular receptor blockers. For intracellular blockers, the incubation time was > 40 minutes during which OGB-1 was fully diffused into the cell. Intracellular block of endoplasmic reticulum IP_3 receptors was accomplished with the broad-spectrum blocker heparin (5 mg/ml) and compared to a separate set of myelin Ca^{2+} imaging experiments from age-matched controls. Combined block of IP_3 and RyRs was achieved with freshly adding heparin, $20 \mu\text{M}$ dantrolene and $10 \mu\text{M}$ ruthenium red (all Tocris) to the intracellular solution. The mitochondrial permeability pore (mPTP) was blocked by adding rotenone ($10 \mu\text{M}$) and cyclosporin A ($20 \mu\text{M}$) to the bath (19 ± 3 minutes). Stock solutions for these two blockers were prepared on the day of the experiment. To ensure sufficient Ca^{2+} transients pharmacology experiments were performed between postnatal day 12 and 21 (average 16 ± 2 days, $n = 45$ cells).

Ratiometric fura-2 Ca^{2+} imaging

As ECFP produces considerable crosstalk when excited at 420 nm we used wild-type littermates from the OL reporter mouse line. For calibration experiments we recorded from satellite OLs in layer 5 (Battefeld et al., 2016) and used $200 \mu\text{M}$ of the ratio metric Ca^{2+} reporter fura-2 (F1200, Thermo Fischer Scientific). The excitation light path was custom designed and fura-2 was excited with two LEDs with peaks at 340 nm (M340L4, Thorlabs) and 420 nm (M420L3, Thorlabs) fitted with bandpass excitation filters 340/22 nm (Semrock) and 420/10 nm (Semrock), respectively. LED collimation was achieved with an aspheric UV passing lens for 340 nm (#33-953, Edmund Optics, York, United Kingdom) and a 1" plano-convex lens (N-BK7, Thorlabs) for 420 nm. Both LEDs were combined into a single light path with a 405 nm dichroic mirror (Di02-R405, Semrock). A field stop was mounted into the excitation light path at a focal length of 17.5 cm from the tube lens. The standard tube lens of U-DPXC1 was replaced with a UV passing plano-convex lens (#48-289, Edmund Optics) and the length of the tube was adjusted accordingly. A dichroic mirror at 458 nm (FF458-Di02, Semrock) reflected excitation light to the sample and passed emission light that was then long passed through a colored glass filter of 455 nm (FGL455, Thorlabs) before being collected with the imaging camera (RedShirtImaging LLC, Decatur, GA, USA). Output current of the LEDs was kept identical for recordings and calibration. We minimized LED output changes by using LEDs equipped with proper cooling (passive heat sinks) and not driving LEDs continuously. The camera generates TTL output pulses at the beginning of each frame and each LED was triggered every other frame and all frames were collected and post hoc separated for the two wavelengths similarly as previously published (Miyazaki and Ross, 2015). Each camera frame was triggered for 12.5 ms and light was on for 10 ms to acquire images for both wavelengths at 40 Hz in a pseudo simultaneous manner. Light intensity was adjusted for each excitation wavelength.

Immunohistochemistry

For immunohistochemistry experiments we used brain slices from the electrophysiology experiments ($\sim 300 \mu\text{m}$ thick). Tissue was fixed with 4% PFA for 20 minutes and washed with PBS. Subsequently slices were blocked in PBS supplemented with 2.5%–5% goat serum and 0.5% Triton X-100 for 1 hour at room temperature. The following primary antibodies were used and incubated at room temperature overnight: streptavidin conjugated Alexa488 (RRID: AB_2336881, S32354), Alexa555 (RRID: AB_2307336, S21381) and Alexa594 (RRID: AB_2313574, S11227, all 1:500, Thermo Fisher), rabbit anti-GFP (RRID: AB_305564, 1:1500, ab6556, Abcam), anti MOG (RRID: AB_1587278, 1:1000, MAB5680, Millipore), anti myelin basic protein (MBP, RRID: AB_92396, 1:250, AB980, Millipore), anti proteo-lipid-protein (PLP, RRID: AB_805413, 1:250, Ab15454, Millipore). Layer 5 neuron morphology was recovered by immunoreaction of biocytin with streptavidin and identification of myelinated axon segments was achieved by co-labeling with MBP, MOG or GFP as described above. Slices were mounted on glass slides and embedded in Vectashield with DAPI (H-1200, Vector Laboratories, Burlingame, CA, USA). Acquisition of z stacks was performed with image size set to 2048×2048 and a $40 \times 1.3\text{NA}$ or $63 \times 1.4\text{NA}$ lens using Leica SP5 or SP8 confocal microscopes equipped with Leica ASF software (RRID: SCR_013673, Leica, Germany).

EM

Tissue for EM from P15 neocortex was obtained from acutely prepared slices that were fixed for 30 min in freshly prepared 5% glutaraldehyde in Na-cacodylate (0.1 M, pH 7.4) and from a transcardially perfused P15 pup using the same fixation solution. No difference

in the *g*-ratio between the two preparation methods was observed ($p = 0.11$, *t* test) and the data subsequently pooled. Slices were cryo-protected in 30% sucrose and once saturated, slices were placed in an aluminum boat, frozen on dry ice and recut at 40 μm with a freezing microtome (1205, Reichert-Jung). Adult tissue (12 weeks, ~P87) was obtained from a transcardially-perfused mouse (5% glutaraldehyde in Na-cacodylate). For perfused samples the somatosensory cortex was carefully dissected after fixation and the tissue was subsequently washed in Na-cacodylate buffer. All samples were rinsed in Na-cacodylate and post fixed for 20 min in 1% OsO₄ supplemented with 1% ferricyanide in Na-cacodylate buffer. Subsequently, the tissue was dehydrated using a gradient of ethanol and acetone and embedded in epoxy resin. Once fully hardened, ultrathin 60 nm sections (Ultracut UCT, Leica) were made and collected on EM grids. Contrasting of the tissue was performed with solutions of lead citrate and 0.5% uranyl acetate (Merck KGaA, Darmstadt, Germany). Sections were sampled with a transmission electron microscope (Tecnai 12, FEI Europe, Eindhoven, Netherlands) and digital images were acquired as 16 bit TIF files (Camera: Veleta, Emiss GmbH, Muenster, Germany; Software: Radius, Olympus).

QUANTIFICATION AND STATISTICAL ANALYSIS

Analysis of Ca²⁺ imaging data

Image analysis was performed with Neuroplex software (RedShirtImaging), Axograph X and Excel (RRID: SCR_016137, Microsoft Corp., USA). When images were acquired with a pulsed LED a script was executed to discard every other frame. Next, regions of interest (ROIs) were manually defined on myelinating processes and background areas. Raw Ca²⁺ fluorescence values were extracted from ROIs and an automated script subtracted the background for each ROI and calculated $\Delta F/F$. For the total fluorescence (F) all data points of an ROI were averaged in one time series. During few experiments, acquisition of traces showed bleaching which could be described by a double exponential function. Bleaching is a non-linear process that not only bleaches cell processes, but also the background. A correction of this exponential bleach was not performed because it was negligible with used LED intensities. For an average peak signal of $10.1 \pm 1.0\%$ $\Delta F/F_0$ the difference with and without bleach correction was measured to be $4.7 \pm 1.2\%$ of the maximum peak ($n = 34$ events, $N = 5$ cells). Excitation light intensities were kept at the lowest possible level to prevent bleaching. Ca²⁺ event amplitude, half-width and kinetics were analyzed in Axograph X (Peak detection). For each event the peak ($\Delta F/F_0$) was calculated as an average of 3 data points relative to the baseline preceding the event (usually 100 to 200 ms). The onset of an event was detected at 25% of the peak. The half-width was determined at 50% of the peak. For presentation, individual events are displayed as ($\Delta F/F_0$) while imaging traces with longer duration are shown as $\Delta F/F$. Kinetics of Ca²⁺ events were determined from single exponential fits for the decay. Calculation of propagation speed for Ca²⁺ events was determined from the Δ -time of the onset at 25% of the peak (starting to terminating ROI) over the distance in μm between the starting and terminating ROI. Random event times were generated in Excel using the RAND function (Figure 5F). Custom-written scripts are available on GitHub (see Key Resources Table).

Calculation of free [Ca²⁺]_i

We calculated the free [Ca²⁺] of various dilutions of our pipette solution by using the online maxchelator tool (RRID: SCR_000459, <http://maxchelator.stanford.edu/CaMgATPEGTA-TS.htm>) that is based on the Chelator program (Schoenmakers et al., 1992). Our intracellular solution for patch-clamp experiments contained ATP, EGTA, Mg²⁺ and traces of Ca²⁺ thus we included a correction factor to obtain a constant concentration of 4 mM Mg²⁺ in all used dilutions. Intracellular binding or transport of Mg²⁺ was not factored into the calculation. Parameters for calculation were set to a recording temperature of 32°C, pH of 7.25 and an ionic strength of 0.29 based on the estimated total free ions in our solution. The free [Ca²⁺] has small increment steps in the nanomolar range to account for the low K_d of fura-2. For a standardization curve on our imaging system we prepared dilutions including 100 μM fura-2 and acquired fluorescence ratios (340/420) for all dilutions *ex situ*. The intracellular Ca²⁺ concentration ([Ca²⁺]_i) was calculated as given by (Grynkiewicz et al., 1985).

$$[\text{Ca}^{2+}] = K_{d(\text{eff})} \times \left(\frac{R - R_{\min}}{R_{\max} - R} \right) \times \left(\frac{S_{f2}}{S_{b2}} \right)$$

K_d was set to 0.22 μM , determined from our calibration experiments, which is similar to previous published K_d for fura-2 (Helmchen et al., 1996; Yoo et al., 1999). R was the ratio (340/420) determined during experiments and R_{\min} and R_{\max} the ratio (340/420) measured with calibration solutions as described. Sf2 is the max and Sb2 the min fluorescence at 420 nm.

Analysis of myelin distribution and g-ratio

For identifying axonal segments and determining the length of co-localization with OL processes, confocal images were analyzed in FIJI (RRID: SCR_002285) (Schindelin et al., 2012) by measuring segment lengths along single axons using the segmented line tool. For *g*-ratio measurements EM images were analyzed in FIJI. Using the line tool the inner axon diameter and outer diameter including myelin were measured and subsequently divided.

Morphological reconstructions

For axonal reconstructions single channel z stacks were loaded into Neuromantic 1.7.5 (RRID: SCR_013597) (Myatt et al., 2012) and the axon proper was manually traced. Z stacks containing the myelin channel were subsequently loaded and traced axons were

manually annotated by assigning unique identifiers for unmyelinated and myelinated segments. Reconstructions were saved in swc format and scaled according to the confocal metadata. Graphical display and pseudo coloring of reconstructed axons was performed using the NEURON environment (RRID: SCR_005393, [Hines and Carnevale, 2001](#)).

Statistical tests

Data was tested for normal distribution with Shapiro-Wilk test. When normal distributed and $n \geq 8$ data was tested with paired or unpaired t test. Not normal distributed data was tested with non-parametric tests. Wilcoxon-signed rank test (WSR) was used for paired datasets and Mann-Whitney U tests (MW) for unpaired data. Distributions were tested with a Kolmogorov-Smirnov test (KS-test). Multiple comparisons were performed with ANOVA and post hoc Tukey-test. The respective tests are indicated in the results. All statistical analysis was performed in Prism 7.0a (RRID: SCR_002798, GraphPad Software Inc, La Jolla, CA, USA). No power analysis was performed to estimate the number of experiments.

DATA AND SOFTWARE AVAILABILITY

Datasets are available upon request to m.kole@nin.knaw.nl. Software scripts written for the imaging analyses are available at <https://github.com/Kolelab/Image-analysis>.